Journal of Microscopy, Vol. 237, Pt 2 2010, pp. 136–147
Received 4 December 2008; accepted 20 July 2009
doi: 10.1111/j.1365-2818.2009.03315.x

High-resolution wide-field microscopy with adaptive optics for spherical aberration correction and motionless focusing

P. KNER*,#, J.W. SEDAT*, D.A. AGARD*,† & Z. KAM‡
**Keck Advanced Microscopy Laboratory and Department of Biochemistry and Biophysics, University of California, 600 16th St., San Francisco, CA 94158, U.S.A.*
†Howard Hughes Medical Institute, University of California, San Francisco, CA 94158, U.S.A.
‡Department of Molecular Cell Biology, Weizmann Institute of Science, Rehovot 76100, Israel

Key words. Adaptive optics, biomedical imaging, microscopy.

Summary

Live imaging in cell biology requires three-dimensional data acquisition with the best resolution and signal-to-noise ratio possible. Depth aberrations are a major source of image degradation in three-dimensional microscopy, causing a significant loss of resolution and intensity deep into the sample. These aberrations occur because of the mismatch between the sample refractive index and the immersion medium index. We have built a wide-field fluorescence microscope that incorporates a large-throw deformable mirror to simultaneously focus and correct for depth aberration in three-dimensional imaging. Imaging fluorescent beads in water and glycerol with an oil immersion lens we demonstrate a corrected point spread function and a 2-fold improvement in signal intensity. We apply this new microscope to imaging biological samples, and show sharper images and improved deconvolution.

Introduction

In vivo fluorescence microscopy is an essential tool in cell biology. A dominant driving force has been the extraordinary ability to study live biological samples made possible by the plethora of fluorescent proteins permitting sub-cellular labelling (Shaner *et al.*, 2005). Despite its tremendous versatility, *in vivo* imaging is limited in practice by the sensitivity of biological samples and fluorophores to photodamage and photobleaching. As a consequence, image quality can be severely compromised by the lack of photons. A recent comprehensive study of several modern commercial microscopes (Murray *et al.*, 2007) shows that wide-field microscopy is the most sensitive technique followed by a 2- to 4-fold reduction in sensitivity for spinning disc microscopy, and then a further sensitivity reduction of 10-fold for laser-scanning confocal microscopy. Because wide-field microscopy captures as efficiently as possible every emitted photon ultimately minimizing the sample excitation dose, it is well suited to *in vivo* imaging in samples where scattering is not too large. Although the out-of-focus photons are in the wrong place, they can be effectively re-assigned to the location of emission by constrained deconvolution algorithms (Swedlow *et al.*, 1997).

To maintain the highest resolution and signal intensity in modern three-dimensional microscopy, high numerical aperture (NA) objectives are used. Unfortunately, high NA objectives only give well-corrected images just below the cover slip. As the focal plane is moved deeper into the sample, the image degrades due to path length errors that arise from differences between the refractive index of the sample and that of the immersion media (depth aberration) and due to path length errors that arise from refractive index variations in the sample itself (sample-induced aberrations). In many samples the dominant aberrations are depth aberrations (Schwertner, 2004). In this paper, we concentrate on the depth dependent aberration which can quickly become serious. Imaging 20 μm into a live sample [index of refraction ~1.36 (Choi *et al.*, 2007)] with an oil immersion lens causes the peak intensity of the point spread function (PSF) to drop 3-fold and the width of the PSF in the axial direction to increase by 2-folds (Gibson & Lanni, 1991).

Because deconvolution requires an accurate knowledge of the PSF, a mismatch between the true PSF and that used for deconvolution will significantly degrade the ability to accurately re-assign the out-of-focus photons to their correct positions. Deconvolution with a depth-dependent PSF has been implemented (Kam *et al.*, 2001; Shaevitz & Fletcher, 2007), but this technique is computationally intensive and can never as fully restore the peak intensity of the original

Correspondence to: P. Kner. Tel: +1 706 542 8966; fax: +1 706 542 8806; e-mail: kner@engr.uga.edu

#Present address: Faculty of Engineering, University of Georgia, Athens, GA 30602, U.S.A.

signal, resulting in sub-optimal signal-to-noise ratio. This is in general true of the many sophisticated post-acquisition image processing algorithms that are available.

The problem of depth aberrations can be solved by matching the sample index and the index of the immersion medium, but this is frequently not feasible or desirable. For example, the index of fixed cells can be matched to that of the immersion oil (Staudt *et al.*, 2007), but this option is not available for live imaging. A water immersion objective can be used to more closely match the index of a live sample; however, this solution merely pushes the point at which aberrations become serious from a few micrometres to a few tens of micrometres, and there are many cases where one would like to image hundreds of micrometres into embryos and live tissue (Wyckoff *et al.*, 2007). Water lenses have a correction collar which is generally used to correct for the cover slip thickness. If they are not carefully adjusted, they will cause the same types of image degradation that they are meant to correct. The collar can be adjusted so that the PSF is optimized not just below the cover slip but at some depth into the sample, but this solution still only corrects the PSF for one specific depth. Above and below this position, the PSF will be distorted.

Based on quantitative simulations, we recently proposed that depth aberrations could be effectively eliminated by correcting the phase of the emitted light in the back pupil plane of the microscope (Kam *et al.*, 2007). Depth aberrations are readily corrected across the entire field of view because the path differences of the emitted light that give rise to the depth aberrations are only dependent on the angle of the emitted light and not on field position. Here we describe our first-generation implementation of this proposal using a deformable mirror (DM) conjugate to the back pupil plane in both the excitation and emission paths of a wide-field fluorescence microscope. Only recently have DMs become sufficiently small for them to be reasonable choices for optical microscopy. We chose a DM (described in the 'Materials and methods' section) capable of large displacements to correct aberrations deep into the sample. To correct depth aberrations 50 μm into an aqueous sample for example, requires a total mirror displacement of 10 μm.

Another benefit to controlling the phase in the back pupil plane of the microscope is that it allows for focusing without perturbing the sample (Wright *et al.*, 2006; Kam *et al.*, 2007; Poland *et al.*, 2008). As discussed below, the phase can be modified to compensate not only for the refractive index mismatch, but for the change in focal plane as well. This can be important for rapid three-dimensional imaging; coupling between the objective and sample through the immersion liquid can induce sample motions when the stage or objective lens is rapidly moved. This problem can be completely avoided by focusing with the DM.

Adaptive optics (AO) has been implemented in confocal microscopy (Booth *et al.*, 2002, 2007) and multiphoton microscopy (Sherman *et al.*, 2002; Marsh *et al.*, 2003; Rueckel *et al.*, 2006) to correct both depth aberrations and sample-induced aberrations on a point-by-point basis and in wide-field fluorescence microscopy with optical sectioning by structured illumination (Débarre *et al.*, 2008). Adaptive optics has also been used to correct for off-axis aberrations in a two-dimensional bright-field microscope to increase the field of view (Potsaid *et al.*, 2005). An important drawback to most schemes that have been proposed so far is that they require several images to be taken to optimize the aberration correction. This presents a serious problem for live imaging in biology because the fluorescence intensities can be weak and susceptible to rapid bleaching. Rueckel *et al.* use backscattered excitation light to measure the wavefront. Booth *et al.* used a modal wavefront sensor which required extra images to measure the wavefront. Potsaid *et al.* use a predictive correction based on the known aberration for a given field position.

Materials and methods

Depth aberration correction

The approach we follow is to correct the depth aberrations with an open-loop predictive algorithm similar to the approach taken by Potsaid *et al.* in correcting off-axis aberrations.

This is possible because the depth aberration can be calculated for a given depth into the sample. The depth aberration is the result of depth-dependent path length differences. Figure 1(a) illustrates the path length difference between a ray from a point source at depth d below the cover slip in a material with index $n_2 < n_1$ and a ray from a point source in a material with $n_2 = n_1$. For an objective that obeys the sine condition (Gu, 1999), the phase correction that must be applied in the back pupil plane is (Booth *et al.*, 1998)

$$\phi = 2\pi \frac{d}{\lambda}\left(n_2\sqrt{1-\left(\frac{(NA)\rho}{n_2}\right)^2} - n_1\sqrt{1-\left(\frac{(NA)\rho}{n_1}\right)^2}\right) \quad (1)$$

where $\rho = n_1 \sin\theta$ is the normalized radial coordinate in the back pupil plane, λ is the wavelength of the emitted light and NA is the numerical aperture. For a sample with internal refractive index variations in addition to the refractive index mismatch at the cover slip, this correction will not be complete.

The DM can also be used to focus into the sample. Figure 1(b) shows the path length difference between a point at the cover slip and a point a depth d below the cover slip. Correcting for this additional path length difference in the back pupil plane accomplishes focusing with depth correction. In this case, the phase correction applied in the back pupil plane is

$$\phi = 2\pi \frac{n_2 d}{\lambda}\sqrt{1-\left(\frac{(NA)\rho}{n_2}\right)^2} \quad (2)$$

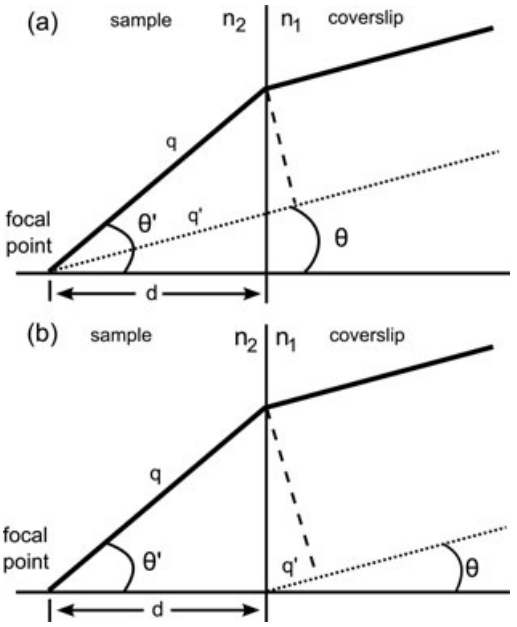

Fig. 1. Ray diagram of the depth aberration. (a) Diagrams the path length difference (n_2q-n_1q') between an unrefracted ray (dashed line) from a point a depth d below the cover slip and a ray that is refracted at the interface (solid line). Compensating for this path length difference in the back pupil plane will correct the spherical aberration. (b) Shows the path length difference (n_2q-n_1q') between a ray from a point just below the cover slip (dashed line) and a ray a depth d below the interface. Compensating for this path length difference in the back pupil plane will focus to a depth d and correct for spherical aberration.

The shape of the DM is then given by

$$f(\rho) = \frac{\phi(\rho)}{2k} \tag{3}$$

where $\varphi(\rho)$ is given by either Eq. (1) or (2). The variable k is the wavevector, ρ and is the normalized radial coordinate of the DM. The factor of 2 accounts for the fact that the change in path length of the light reflecting off of the mirror is twice the mirror displacement.

Microscope design

We have built a microscope to apply the correction given by Eqs (1) and (2) to a DM conjugate to the back pupil plane of the objective. Figure 2 shows the layout of the microscope. The tube lens (180 mm focal length (Olympus, Tokyo, Japan)) and lens f_1 (350 mm achromat (OptoSigma, Santa Ana, CA, U.S.A.)) serve to reimage the back pupil plane of the objective (Olympus, 60×, 1.42 PlanApo N) onto the DM (Mirao52d (Imagine Optic, Orsay, France). Lens f_2 (1500 mm singlet (Newport Corp., Irvine, CA, U.S.A.), or 800 mm achromat, OptoSigma) then creates the corrected image on the charge-coupled device (CCD) camera. The magnification of the back pupil plane of the 1.42 NA 60× oil objective onto the DM overfills the DM so that the DM acts as an aperture that limits the system NA to 1.285. Focusing into the sample away from the cover slip, the NA cannot be greater than the sample index of refraction (by definition) so we chose a NA less than the limit inherent when using water, 1.333. Choosing a lower NA also reduces the total throw required by the mirror, but this NA is still larger than the NA of most water immersion objectives, 1.2. Lens f_1 is chosen to match the desired NA to the DM diameter, and lens f_2 is chosen so that the total magnification of the system, $M_{\text{obj}}(f_2/f_1)$, samples the object at greater than the Nyquist frequency on the CCD camera; here $d_{\text{pixel}} = 50.6$ nm or 94.6 nm in sample coordinates. We oversample so that we accurately measure the PSF without having to interpolate the data. The CCD camera is from Astronomical Research Cameras, Inc. (San Diego, CA, U.S.A.) and uses a cooled CCD57-10 chip with a 13 μm pixel size from e2v Technologies (Chelmsford, U.K.). The additional components between the tube lens and the CCD camera reduce the light efficiency of the system by no more than 22%. This could be reduced further by using dielectric mirrors instead of metallic mirrors.

The excitation light, at 488 nm from an Innova laser (Coherent, Santa Clara, CA, U.S.A.), passes through an optical shutter (UniBlitz, Rochester, NY, U.S.A.) and is focused onto a rotating diffuser (Physical Optics, Torrance, CA, U.S.A.) to remove spatial coherence. The light is then coupled into a multimode fibre (600 μm core, 0.22 NA (Ocean Optics, Dunedin, FL, U.S.A.). The output end of the fibre is imaged onto the DM with lenses f_{ex1} (10 mm achromat, PAC310 Newport Corp.) and f_{ex2} (250 mm achromat, PCA067 Newport Corp.) and inserted into the main optical path with dichroic 1 (FF495-Di01 (Semrock, Rochester, NY, U.S.A.)). Thus, the excitation is also corrected for the depth aberrations. Although this is not critical for wide-field illumination, correction of the excitation is equally as important as correction of the emission in techniques such as structured illumination microscopy (Gustafsson, 2000).

The final optical path in the system injects a 632 nm HeNe laser into the system to monitor the shape of the DM. The beam from the HeNe laser is cleaned and expanded with a pinhole and then collimated. The light is inserted into the optical path with dichroic 2 (Semrock FF579/644-Di01). It then follows the optical path until it is taken out of the main optical path with dichroic 3 (Semrock FF 579/644-Di01) and sent to a Shack–Hartmann wavefront sensor (Haso 32, Imagine Optic, Orsay, France). Lenses f_{sh1} (300 mm achromat) and f_{sh2} (100 mm achromat) demagnify the beam to image the DM onto the lenslet array.

The microscope slide is mounted above the objective on a custom-designed mount that uses a Newport 462 *xyz*-stage. *Z*-stacks are taken with a piezo stack attached to the *z*-axis micrometer (P-810 piezo and E661.CP controller (Physik Instrumente, Karlsruhe, Germany)), and the stage position is measured with a capacitive sensor (NS2000-L (Queensgate, Torquay, U.K.)).

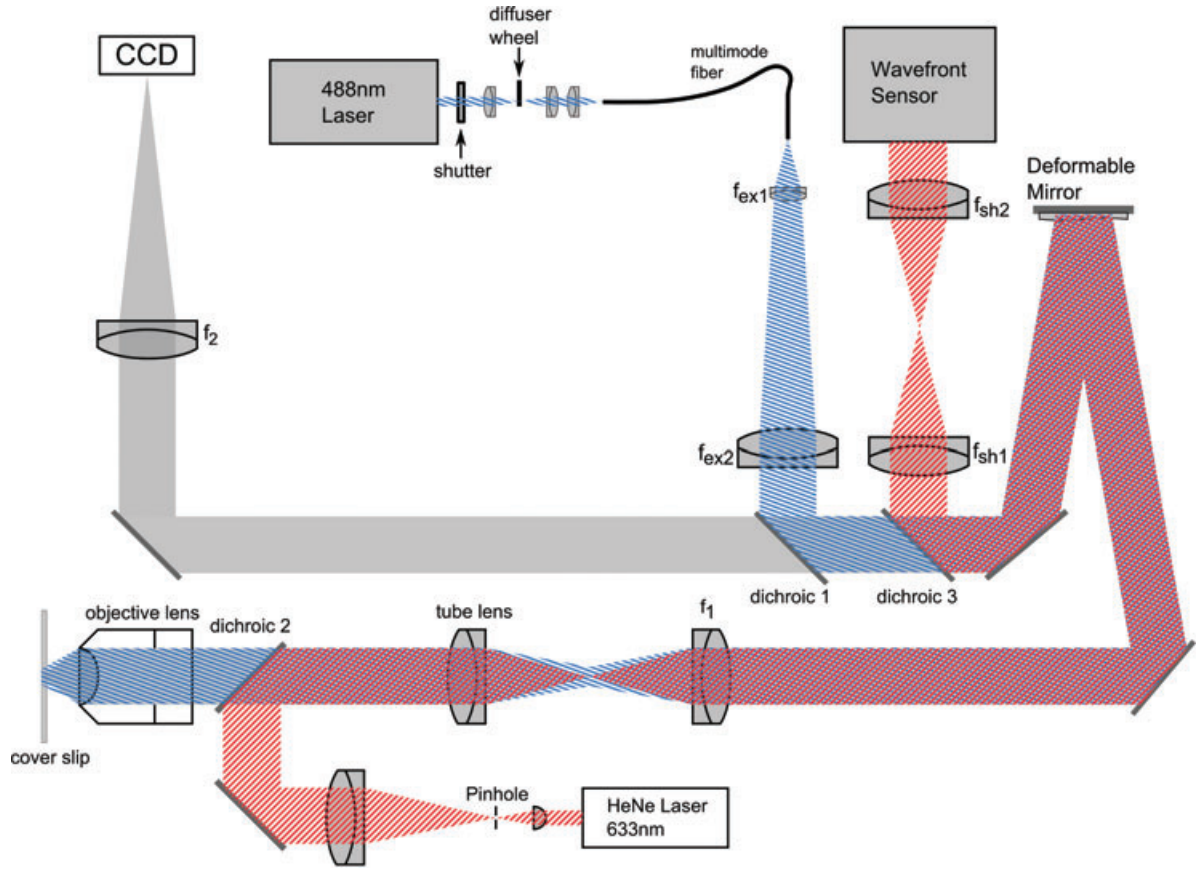

Fig. 2. Microscope layout. Grey represents the emission path. The blue striped beam is the excitation light and the red striped beam is the reference beam. See text for details.

Three-dimensional image stacks

All the three-dimensional data stacks were taken using the piezo for focusing through the sample except the data for Figs 10 and 11 in which the focusing was performed by the DM. In three-dimensional image stacks in which Eq. (1) was used to correct the depth aberration, the correction was adjusted for each depth so that the PSF is corrected throughout the sample and not just at one particular depth. The only exception to this is the images of a bead in Figs 4 and 6, where the phase correction was set to the depth of the centre of the bead and not adjusted for the three-dimensional data stack.

Deformable mirror control

For the DM, we chose the Mirao52D from Imagine-Optic (www.imagine-optic.com) because it is capable of large displacements and thus permits the correction of aberrations deep into a sample. The 15-mm-diameter mirror has 52 actuators on a square grid with 2.5 mm spacing. The mirror is capable of a maximum displacement of ± 75 μm for the focus mode (Z_2^0) and ± 8 μm for the first order spherical aberration (Z_4^0). The mirror can take the shape of any Zernike mode through order 4 with a root-mean square (rms) wavefront error of less than 20 nm. Because the mirror cannot set the higher order terms, the Strehl ratio will degrade with depth, as the amount of higher order spherical terms needed to fit the correction (given by Eq. 2) increases. Thus, the maximum depth the mirror can correct will be limited by the residual aberrations and not the maximum displacement of the focus mode.

We control the mirror by measuring the wavefront of the HeNe laser with the wavefront sensor (reference path in Fig. 2). We reference the wavefront to a measurement with all actuators set to zero, and then measure the wavefront on a 32×32 lenslet array for each of the 52 actuators activated individually, yielding a 1024×52 matrix. To set a desired mirror shape, we use the standard singular value decomposition technique (Gavel, 2003) to determine the matrix S which will yield the actuator values for a desired wavefront. Typically, we only retain the first 45 singular values.

Sample preparation

To estimate the PSF, we imaged 200-nm-diameter Yellow-Green fluorescent beads (F-8811, Molecular Probes, Inc.,

Eugene, OR, U.S.A.). Because a bead is smaller than the diffraction spot, its image represents a good approximation for the PSF of the microscope. The beads are dispersed in water at a concentration of 2% by weight and were diluted by an additional factor of 10^6 in water to a concentration of 3.9×10^6 beads/ml (Fluospheres Fluorescent Microspheres Application Note, Molecular Probes, Inc.). To image beads at 0 depth (on the cover slip), 15 μl of bead solution were dried on a #1.5 cover slip and mounted on a slide with 5 μl of glycerol. To image beads below the cover slip, #2 cover slips were glued to a slide on either side of a #1.5 cover slip using optical adhesive (Optical Adhesive 61 (Norland, Cranbury, NJ, U.S.A.)). The #2 cover slips serve as a support. 200 nm beads were dried on the centre cover slip and on a 40 × 20 mm #1.5 cover slip. A total of 25 μl of a water/glycerol mixture was put on the slide and the larger cover slip was placed on top and sealed with nail polish. The relative concentration of water and glycerol in the mixture was adjusted to yield an index of refraction of 1.42 for the mounting solution (Newman, 1968). The distance between the top cover slip and the slide varied between 45 and 75 μm.

To image beads at a variety of depths (Fig. 10), a 2% w/v solution of 200 nm YG beads was diluted by a factor of 1000 and mixed at a concentration of 1:1 with a solution of 2% low-temperature Agar. Approximately 30 μl of the solution was pipetted onto a microscope slide and immediately covered with a #1.5 cover slip and sealed with nail polish.

B16F10 mouse cells were grown on Fibronectin coated #1.5 cover slips and were stained with Alexa488-phalloidin to label the actin following the protocol developed by Cramer and Desai ('Fluorescence Procedures for the Actin and Tubulin Cytoskeleton in Fixed Cells', http://mitchison.med.harvard.edu/protocols/gen1.html). The cover slips were then mounted on slides with Phosphate Buffered Saline (PBS) and sealed with nail polish.

Live worms expressing a Green Fluorescent Protein (GFP) sur-5 construct were mounted on agar in M9 buffer containing 1 mM Levamisole and sealed with #1.5 cover slips. Bladder cancer cells from endothelial bladder carcinoma cancer cell line UMUC3 (#CRL-1749 (American Type Culture Collection, Manassas, VA, U.S.A)) infected with the Lentivirus GFP construct of the protein Telemeric Repeat binding Factor 1 (TRF1) were grown on #1.5 cover slips and then mounted on slides with PBS buffer and sealed with nail polish.

Eye imaginal discs from a third instar larvae of the w1118; P{wmc, CIDGFP} fly line (Henikoff *et al.*, 2000) were dissected into a drop of PBS buffer on a cover slip (Wolff, 2000). Before dissection, the #1.5 cover slip was glued to a metal slide with UV cured epoxy. The drop with the discs was covered with a gas-permeable membrane for the purpose of flattening the tissues and gently pressing them against the cover slip. The top of the slide over the cover slip was then sealed with a clear plastic cover to prevent evaporation of the buffer.

Deconvolution

The deconvolution was performed using the AIDA software package (Hom *et al.*, 2007). We used the myopic deconvolution option in AIDA, allowing the PSF to vary to optimize the reconstructed object, and the initial guess was a Wiener-filtered version of the image. The maximum changes in the PSF were 20% of the maximum value. The deconvolution of a 256 × 256 × 64 pixel image stack took approximately 30 min on a Pentium III computer.

Results

Deformable mirror performance

Figure 3(a) shows the mirror shape and residual error for focusing a depth of 5 μm into water with an oil immersion lens. The desired shape of the mirror given by Eq. (2) cannot be set exactly by the mirror and there is a 20 nm residual rms error in the wavefront. Figure 3(b) shows the residual rms error as a function of the depth. This effectively sets the upper limit to the depth that can be corrected for a given NA and refractive index mismatch. Another important aspect of the DM performance is 'print-through' which is any residual non-flat structure at the array spacing due to the manufacturing process. The print-through will diffract light because it is a regular pattern and results in satellite peaks in the PSF as discussed below.

Imaging beads

Figure 4 shows an image of a 200 nm Yellow-Green bead at the cover slip. Because the bead diameter is just below the microscope resolution, the image of the bead is a reasonable approximation of the PSF of the microscope (Hiraoka *et al.*, 1990). The finite size of the bead should increase the full-width at half-maximum (FWHM) of the PSF by 15% and reduce the contrast of the rings in the airy disk. As can be seen from the figure, the PSF is well corrected with a FWHM of 270 nm which is 15% larger than the theoretical FWHM of 234 nm for 520 nm emission light with an NA of 1.285 and a 200 nm bead. This is comparable to the PSF measured with a silver coated flat mirror in place of the DM. The FWHM of the PSF in axial direction is 700 nm.

Although the general behaviour is as expected a grid of spots around the central peak is apparent in the in focus PSF, Fig. 4(b); each of these small peaks is about 1% of the maximum intensity of the central spot. This feature is due to the print-through mentioned above which diffracts light away from the central peak into spots a distance $f_1(\lambda/\Lambda)/M_{\text{obj}}$ (in sample coordinates) away from the centre of the PSF, where Λ is the actuator spacing. A DM with more actuators would produce spots farther away from the central peak. A more significant consequence of print-through is observed

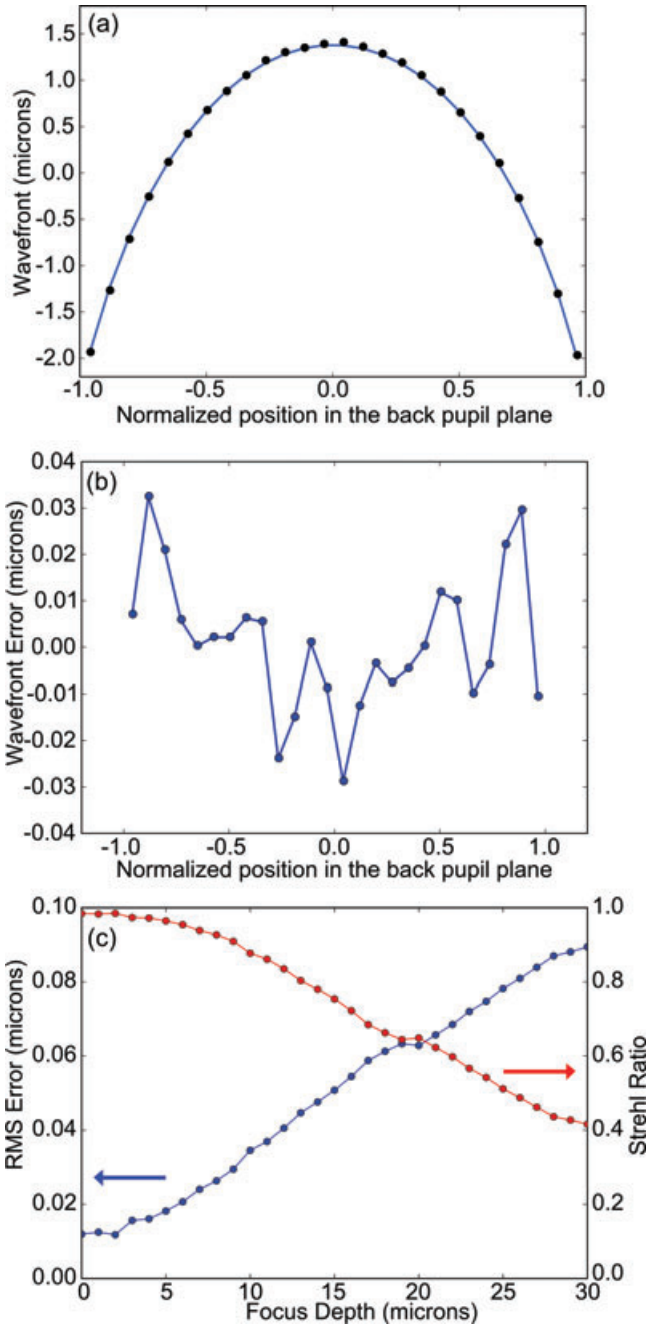

Fig. 3. (a) Cross-section of measured mirror shape (black circles) compared to the theory given by Eq. (2) (blue line) for $d = 5$ μm with $n_1 = 1.512$, $n_2 = 1.333$, $NA = 1.2$. (b) Difference between measurement and theory from (a). (c) Measurement of wavefront error (blue circles, left axis) as a function of the shape applied to the DM. The corresponding Strehl ratio calculated using the Marechal equation is given by the red line on the right axis. The shape is given by *Eq. (3)* with $n_1 = 1.512$, $n_2 = 1.333$, $NA = 1.285$ and depth given by the x-axis. 45 singular values were used in the singular value decomposition for these measurements.

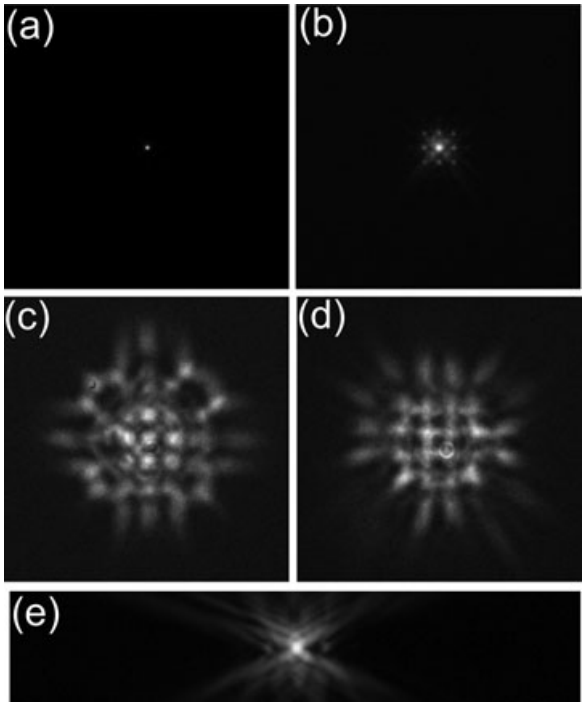

Fig. 4. PSF of the microscope measured at the cover slip. (a) PSF in focus scaled to maximum intensity. The images are 24 μm × 24 μm. (b) PSF in focus, logarithmic scale. A series of faint peaks are visible around the central PSF due to diffraction from the mirror print-through. (c) PSF 6 μm out of focus away from the cover slip. (d) PSF 6 μm out of focus towards the cover slip. (e) *xz*-cross-section of the PSF on a logarithmic scale. The image is 24 μm × 10 μm.

in the out-of-focus light in the PSF. As can be seen in Fig. 3(c) and (d), the out-of-focus blur is modulated by a periodic square pattern due to the square actuator array. The shape of the PSF is different above and below the focal plane because the print-through is not symmetric in the axial direction. Far away from focus, because of Fraunhoffer diffraction, the PSF starts to resemble the print-through. The effect of print-through is an important difference between the use of adaptive optics in wide-field imaging and in confocal and two-photon imaging where the pinhole or nonlinearity effectively removes all but the central peak of the PSF. We have used phase-retrieval (Hanser *et al.*, 2004) to calculate the wavefront in the back-pupil plane from the PSF. The DM print-through is clearly visible in the phase of the wavefront with a magnitude of roughly 30 nm as shown in Fig. 5.

To simulate the effects of imaging deep into living tissue, Fig. 6 shows images of a 200 nm bead 67 μm deep in a glycerol/water mixture having index of refraction 1.42. As expected, images taken first without correcting for the depth aberration (with the DM flat, Fig. 6a, c, e) show strong spherical aberration. Images taken with the shape of the DM set by Eq. (1) (Fig. 6b, d, f) show a more symmetric PSF similar to that just below the cover slip. As is clear from Fig. 6, the correction

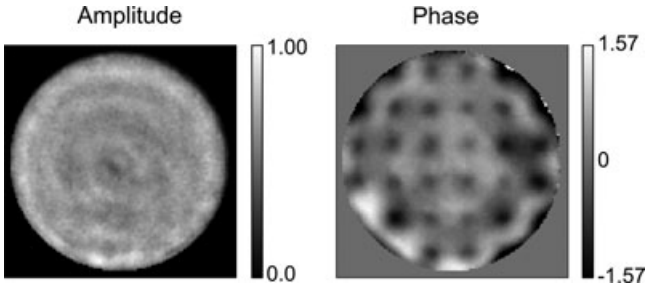

Fig. 5. Back pupil plane calculated by phase retrieval from the three-dimensional image of a 200 nm bead at the cover slip. Amplitude (left) and phase scaled from $-\pi/2$ to $\pi/2$ radians (right). The DM print through is clearly visible. 20 of the actuators are at the edge of the mirror and therefore do not produce a print-through bump.

achieves several important results. First, the peak intensity of the corrected images is a factor of two larger than the uncorrected image. Because the uncorrected image was taken first, any bleaching of the sample (measured from similar data to be 4% per image stack) would result in a higher intensity for the uncorrected image, underestimating the improvement obtained using the DM. Second, the correction removes the low intensity 'pedestal' of light around the main peak in the uncorrected image and returns it to the central peak as can be clearly seen in the logarithmic scale image, Fig. 6(c) and (d). Third, the shape of the PSF (compare Fig. 6e and f) after correction is almost exactly the same as that of the PSF at the cover slip, which should result in much better deconvolution results. Lastly, the width of the peak in the axial direction is significantly reduced after correction resulting in a higher axial resolution (Fig. 6h). The lateral plane FWHM of the peak is not significantly changed by the correction as seen in Fig. 6(g). This is because the depth aberrations do not increase the width of the central peak very much. The aberrations create a broad pedestal upon which the central peak sits (Fig. 6c and d). Figure 6(i) and (j) show simulations of the PSF in the axial direction for parameters corresponding to the measured data. Figure 6(i) simulates a PSF 65 μm below the cover slip with the same refractive index mismatch and Fig. 6(j) simulates a well-corrected PSF at the cover slip. As can be seen in the figure, the agreement is quite good. The main difference is that in the experiment the correction increases the peak intensity by 2.05. In theory, the peak intensity of the corrected PSF is 3.75 times higher than the aberrated PSF.

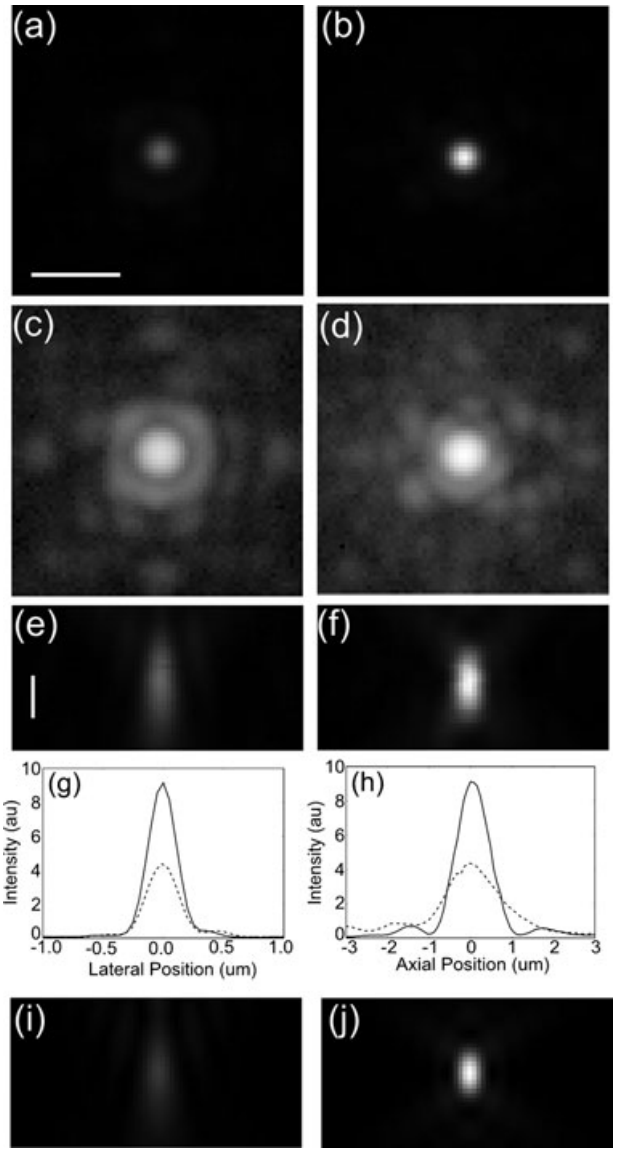

Fig. 6. Images of a 200 nm bead 67 μm below the cover slip in a water/glycerol mixture with $n = 1.42$. (a) Uncorrected image of in-focus plane. (b) Corrected image of in-focus plane: same scale as (a). (c) and (d) are the same as (a) and (b), respectively, but on a logarithmic scale. (e) and (f) are cross-sections through the focal plane on a linear scale. The scale bars are 1 μm. (g) and (h) are line profiles through of the intensity through the centre of the bead along a lateral and the longitudinal axis, respectively. The dashed line is from the uncorrected image and the solid line is from the corrected image. (i) and (j) are simulations of the PSF. (i) corresponds to the uncorrected PSF 65 μm into a material with index 1.42 using a 1.2NA objective with a 1.512 refractive index immersion oil. (j) is a simulated PSF at the cover slip. The peak intensity for (j) is 3.75 times the peak intensity for (i).

Biological imaging

Of course, the goal of using adaptive optics in fluorescence microscopy is to correct images of biological samples. In this section we will show results demonstrating the correction of spherical aberration in biological samples, but the results are less dramatic than the results on a single bead because the biological sample introduces scattering and other aberrations. Figure 7 shows uncorrected (Fig. 7a) and corrected (Fig. 7b) lateral images 24 μm below the cover slip of UMUC bladder cancer cells with GFP-TRF1 labelled telomeres. Although the intensity of the cell autofluorescence is not increased by the correction of the depth aberrations, the GFP-TRF1 signal is

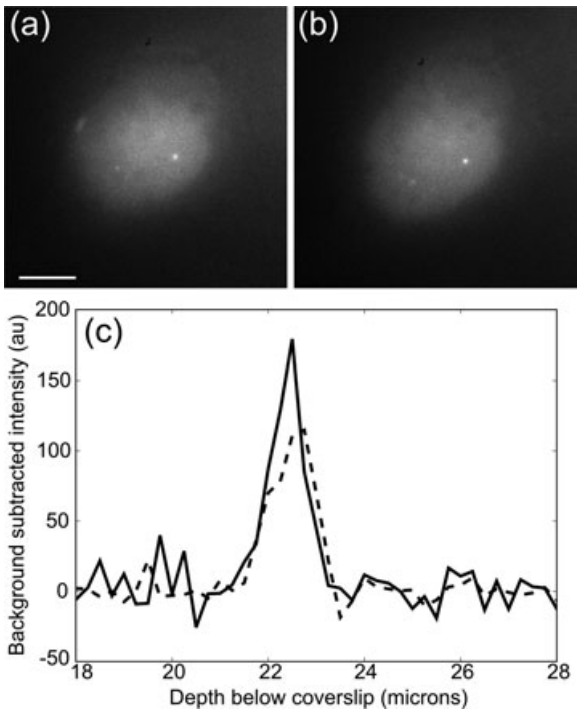

Fig. 7. Images of GFP-TRF1 labelled telomeres in UMUC bladder cancer cells. (a) Uncorrected images 23 μm below the cover slip. (b) Depth aberration corrected 23 μm below the cover slip. The correction assumed a sample index of 1.38 (c) Background subtracted profiles through the labelled telomere (bright spot in images a and b) along the axial direction. The dashed line is from the uncorrected image a, and the solid line is from the corrected image (b). The peak intensity in the corrected image is 60% larger over the background. The scale bar is 5 μm.

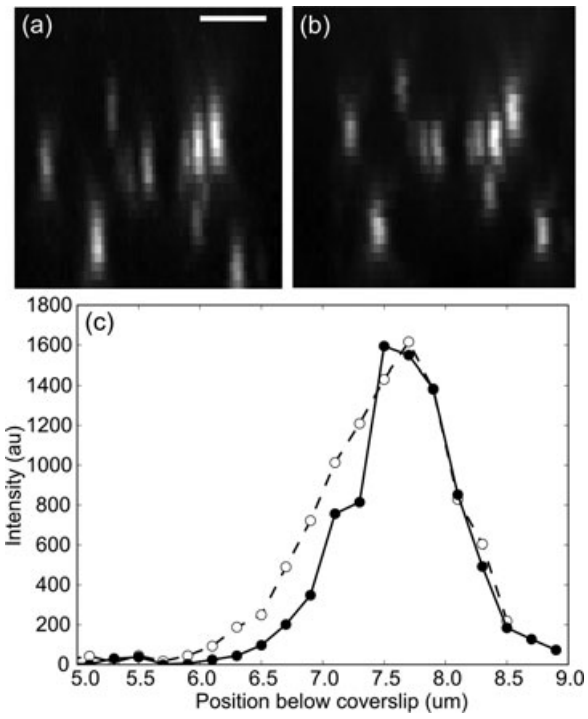

Fig. 8. GFP labelled centromeres in eye Imaginal Discs in Drosophila embryos. Scale bar is 2 μm. (a) Maximum intensity projection of uncorrected three-dimensional data stack. Vertical is the axial direction. The top of the image is 2 μm below the cover slip and the bottom is 9 μm below the cover slip. (b) Maximum intensity projection of a depth aberration corrected data stack. The correction assumed a sample index of 1.38. (c) Line profiles along the axial direction for uncorrected (dashed line, open circles) and corrected (solid line, solid circles) images of a GFP labelled centromere.

brighter by 60% after subtracting the broad autofluorescence signal (Fig. 7c). Because the aberrations spread out the energy but do not remove it, we would not expect a spatially broad signal from the autofluorescence or from a thin fluorescent sheet to be improved by correcting the depth aberration in a wide-field microscope because the integrated intensity is unchanged. Figure 8 shows another example, GFP labelled centromeres in eye Imaginal Discs in Drosophila embryos. In this sample, correcting the depth aberration did not increase the intensity of the signal from the GFP centromeres, but the FWHM of the centromere images in the axial direction are smaller by 27% in the axial direction which can be seen in Fig. 8.

Because adaptive optics corrects the PSF throughout the sample (the DM shape is adjusted according to Eq. 1 at each depth), it should greatly improve the ability of deconvolution algorithms to remove the blurring of the object caused by the PSF; this is because the PSF is now constant throughout the image and matches the PSF taken at the cover slip which is used for deconvolution. This is demonstrated in Fig. 9, which shows the deconvolution of images of actin labelled with Alexa488-Phalloidin in B16F10 cells. The deconvolved image, Fig. 9(d), of the AO-corrected data shows significantly less background than the deconvolved image of the uncorrected data, Fig. 9(b). Interestingly the images before deconvolution (Fig. 7a and c, which are the uncorrected and corrected images, respectively) do not look as different. These images are *xy*-sections 4.4 μm below the cover slip and show actin labelling in cell–cell junctions.

In addition to correcting the depth aberration, the DM also has the capability to focus into the sample as described by Eq. (2). Figure 10 is an example of using the DM to focus through 200 nm beads in an agarose solution. It is clear from the maximum intensity projections in Fig. 10(a) and (b) that the DM correctly focuses through the sample because the same beads can be seen in both images. Unfortunately focusing with the DM adds aberrations because the remote focusing configuration is sensitive to aberrations in the optical components between the sample and the DM. This is because the beam diameter before the DM changes as a function of depth. If there is an aberration in the fold mirror before the DM, it can be corrected with the DM for imaging just below the cover slip, but this correction will not work for imaging deeper into the sample because the beam diameter on the fold mirror will have changed. Thus the improvement

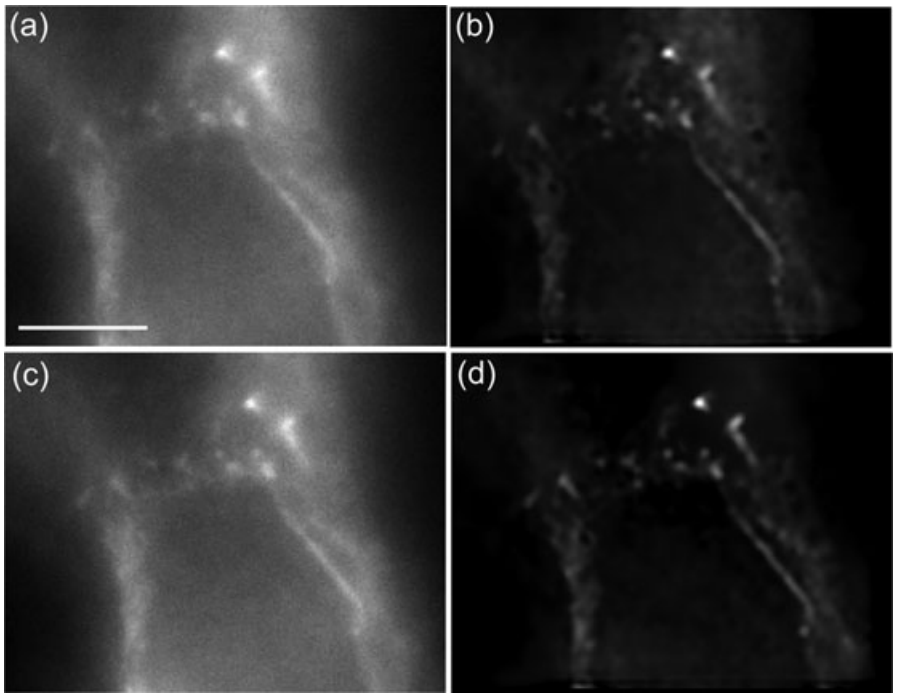

Fig. 9. Deconvolved images of alexa488-phalloidin labelled B16F10 mouse cells. Images are 4.4 μm below the cover slip. (a) Uncorrected image. (b) Uncorrected deconvolved image (c) image corrected by adaptive optics. The correction assumed a refractive index of 1.38 (d) image corrected by adaptive optics after deconvolution. The scale bar is 5 μm.

due to depth correction may be negated by aberrations in optical components that are uncorrected as the system is focused into the sample. Figure 11 is an example of using a DM to focus through an adult *C. elegans* worm expressing a GFP sur-5 construct. The images in Fig. 11(a) are from a three-dimensional data stack taken using the DM to focus in *z*, and are comparable to the images taken in Fig. 11(b) using mechanical focusing. The same features are clearly visible in both images although the level of background fluorescence has changed.

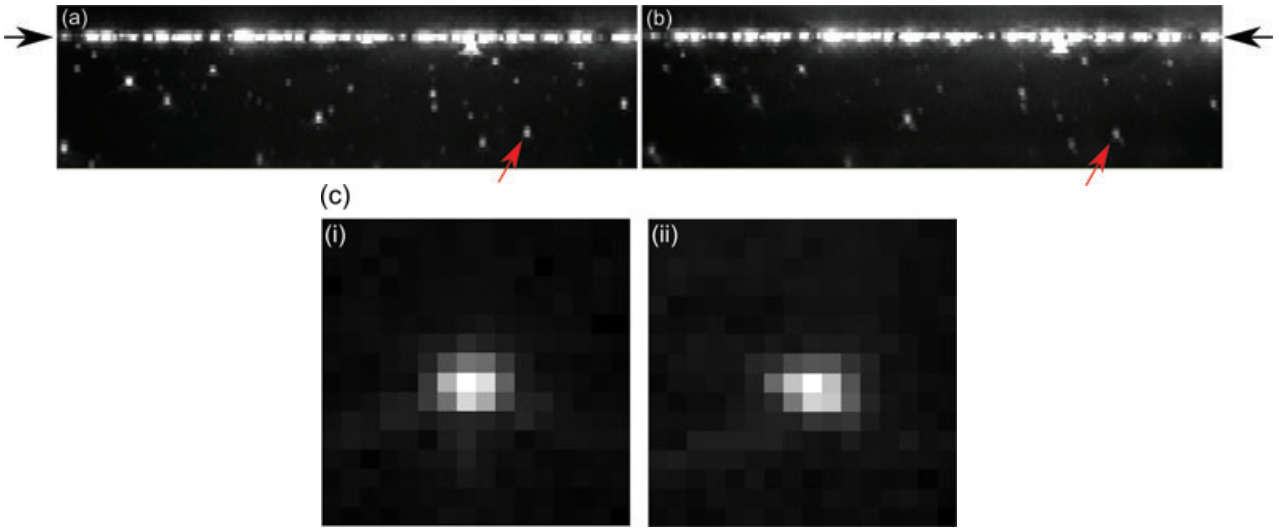

Fig. 10. Maximum intensity projections of three-dimensional data stacks of 200 nm beads in agarose. The vertical direction is the axial direction and the total height of each image represents 22.5 μm. The width of each image is 34 μm. The arrows point to the position of the cover slip. Image (a) was taken using the piezo for focusing. Image (b) was taken using the DM to focus. The DM shape was set by Eq. (2) using a sample refractive index of 1.34. (c) Shows close-ups, (i) and (ii), of the bead indicated by the red arrows in (a) and (b). The images are 1.6 μm × 8 μm (16 × 16 pixels) cross-sections in the *xz*-plane, scaled to maximum intensity.

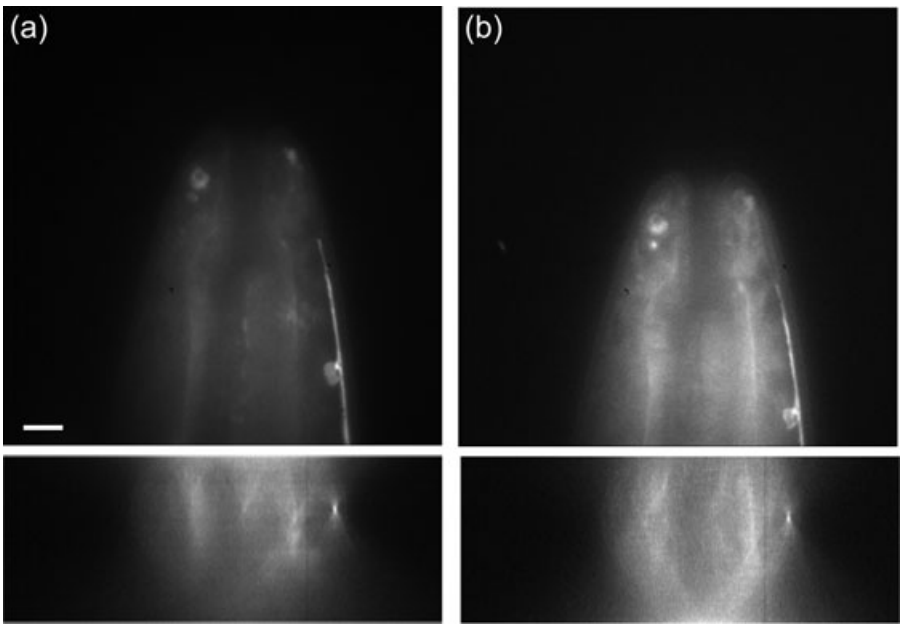

Fig. 11. Comparison of images taken by focusing with the DM (a) and mechanical focusing (b). Images are of *C. elegans* expressing a GFP sur-5 construct; the bright feature along the right side is the ventral nerve cord. The top images are taken 6 μm below the cover slip and the bottom images are *xz*-cross-sections. The difference in image intensity is due to photobleaching. Each image is scaled to its maximum intensity. A sample refractive index of 1.36 was assumed for focusing with the DM using Eq. (2). The scale bar is 2 μm.

Discussion

Correcting depth aberrations with a DM improves both the peak intensities and the deconvolution of images taken below the cover slip by removing the depth aberration. This allows the use of fast space-invariant deconvolution algorithms instead of depth-dependent algorithms. This is significant because it improves both the signal-to-noise ratio and the resolution in biological imaging where photons are in short supply. Unfortunately, the performance does not yet achieve what is theoretically possible.

Although the correction of a bead in glycerol, Fig. 6, shows an impressive improvement in intensity due to the correction, the factor of 2 increase in signal is still less than the factor of 4 that should be possible based on the theoretical decrease in intensity predicted by the depth, NA and index of refraction mismatch. There are two important factors that contribute to this effect. The first is the effect of uncorrected aberrations from the sample and the optical path, which decrease the maximum intensity at the cover slip, but in a way that does not add linearly to the depth aberration. Thus only a fraction of the dispersed photons can be restored to the central peak. In closed loop AO systems, system aberrations are automatically compensated at each position (Wright *et al.*, 2007), but in an open-loop system this is not possible. The second factor is the inability of the mirror to precisely conform to the shape given by Eq. (1). The residual error of the mirror shape increases with depth (see Fig. 3c) so that as the imaging plane goes deeper and the possibility for improvement becomes greater, the improvement in peak intensities decreases. To address the first problem we must reduce the residual aberrations in the system as much as possible. The objective and tube lens will not be perfect (Juskaitis, 2007), and the mirrors used in our system are also a potential source of aberrations. Most silver mirrors are specified to have a rms surface flatness of $\lambda/10$. According to the Marechal criterion (Hardy, 1998), this will result in a Strehl ratio of roughly 0.6. Thus having a few mirrors in the system can be a significant source of aberration.

Similar to the residual aberrations in the optical train, sample-induced aberrations can affect the performance of the system in a nonlinear way and will affect the measured performance of the microscope in correcting depth aberrations. Scattering will also affect the ability of the microscope to recover the intensity lost since scattering will disperse the light in a random way so that it cannot be imaged.

Another important feature of three-dimensional wide-field microscopy is the out-of-focus light present in the three-dimensional PSF. As can be seen in Figs 4 and 5, the PSF of the system contains a weak grid of points outside the central peak due to the print-through. In confocal microscopy, only light in the central peak is accepted by the pinhole; therefore, the PSF should not be substantially altered although the intensity measured inside the pinhole is still less than ideal. In wide-field microscopy, the structure in the PSF can be visible in the image. Deconvolution is important for removing this structure, and the AIDA deconvolution package works well but could be further modified to explicitly address such features that arise in adaptive optics. Myopic deconvolution, allowing the PSF

to vary under a harmonic constraint along with optimization of the reconstruction, is an option in AIDA, and it would be interesting to tailor the PSF constraint for the case of adaptive optics where the spatial frequency of the print-through is known, but its exact structure could be optimized to account for details of the PSF.

The ability to focus with the DM is very exciting for live imaging because it enables the acquisition of three-dimensional data rapidly without any movement or disturbance of the sample; DMs have typical response times of better than 200 Hz and modern cooled CCD cameras can capture 256×256 pixel images at faster than 60 fps. An active focus locking system has been implemented with adaptive optics by (Poland *et al.*, 2008) at over 200 Hz. Other motionless refocusing techniques are either not as fast (Tsai *et al.*, 2007) or cannot correct for the refractive index mismatch (Botcherby *et al.*, 2007). The optical system can be redesigned to use optical components with better surface quality, and there is also the possibility that the system could be calibrated to correct for the aberrations at every focus position.

There are many modifications to the microscope design that we discuss here that could improve correction of depth aberrations and extend the design to the correction of sample-induced aberrations. A DM with more actuators could be used to more faithfully approximate the depth correction term given by Eq. (1). One difficulty with this is that the dense-actuator devices typically can deform by at most a few wavelengths. To get around this difficulty, a microscope with two DMs in a 'woofer-tweeter' configuration could be designed using one large-throw actuator mirror and one dense-actuator low-throw mirror or liquid crystal device (Wright *et al.*, 2006). Another possibility is to design a DM specifically to focus with a shape given by Eq. (2). This DM could be designed to have only one or at most a few actuators to control the shape and would not have the problems with print-through from a grid of actuators, allowing it to be smaller and faster as well. Lastly, the ultimate goal of applying adaptive optics in microscopy is to correct all aberrations including those introduced by the refractive index variations of the sample itself. Thus, inserting additional DMs conjugate to several planes in the sample itself for correcting sample-induced variations over the field of view, as simulated theoretically (Kam *et al.*, 2007), is an important future goal.

Acknowledgements

We thank Kaveh Ashrafi, Xeuying Wang, Yuri Strukov, Pete Carlton and Hesper Rego for help in preparing biological samples. ZK is the Israel Pollak Professor of Biophysics. This work was supported by NIH Grants GM25101 (JWS) and GM31627 (DAA), the National Science Foundation through the Center for Biophotonics Science and Technology under Cooperative Agreement No. PHY 0120999, and by the Keck Laboratory for Advanced Microscopy. We thank Steve Lane at the Center for Biophotonics Science and Technology and members of the National Science Foundation Science and Technology Center for Adaptive Optics at the University of California at Santa Cruz for helpful discussions.

References

Booth, M.J. (2007) Wavefront sensorless adaptive optics for large aberrations. *Opt. Lett.* **32**, 5–7.

Booth, M.J., Neil, M.A.A. & Wilson, T. (1998) Aberration correction for confocal imaging in refractive-index-mismatched media. *J. Microsc.* **192**, 90–98.

Booth, M.J., Neil, M.A., Juskaitis, R. & Wilson, T. (2002) Adaptive aberration correction in a confocal microscope. *Proc. Natl. Acad. Sci. USA* **99**, 5788–5792.

Botcherby, E.J., Juskaitis, R., Booth, M.J. & Wilson, T. (2007) Aberration-free optical refocusing in high numerical aperture microscopy. *Opt. Lett.* **32**, 2007–2009.

Choi, W., Fang-Yen, C., Badizadegan, K., Oh, S., Lue, N., Dasari, R.R. & Feld, M.S. (2007) Tomographic phase microscopy. *Nat. Methods* **4**, 717–719.

Débarre, D., Botcherby, E.J., Booth, M.J. & Wilson, T. (2008) Adaptive optics for structured illumination microscopy. *Opt. Exp.* **16**, 9290–9305.

Gavel, D. (2003) Suppressing anomalous localized waffle behavior in least squares wavefront reconstructors. *Proceedings of SPIE.* SPIE, Waikoloa, HI, USA.

Gibson, S.F. & Lanni, F. (1991) Experimental test of an analytical model of aberration in an oil-immersion objective lens used in three-dimensional light microscopy. *J. Opt. Soc. Am. A* **8**, 1601–1613.

Gu, M. (1999) *Advanced Optical Imaging Theory*, Springer Verlag, Berlin.

Gustafsson, M.G. (2000) Surpassing the lateral resolution limit by a factor of two using structured illumination microscopy. *J. Microsc.* **198**, 82–87.

Hanser, B.M., Gustafsson, M.G., Agard, D.A. & Sedat, J.W. (2004) Phase-retrieved pupil functions in wide-field fluorescence microscopy. *J. Microsc.* **216**, 32–48.

Hardy, J.W. (1998) *Adaptive Optics for Astronomical Telescopes.* Oxford University Press, New York.

Henikoff, S., Ahmad, K., Platero, J.S. & van Steensel, B. (2000) Heterochromatic deposition of centromeric histone H3-like proteins. *Proc. Natl. Acad. Sci. USA* **97**, 716–721.

Hiraoka, Y., Sedat, J.W. & Agard, D.A. (1990) Determination of three-dimensional imaging properties of a light microscope system. Partial confocal behavior in epifluorescence microscopy. *Biophys. J.* **57**, 325–333.

Hom, E.F., Marchis, F., Lee, T.K., Haase, S., Agard, D.A. & Sedat, J.W. (2007) AIDA: an adaptive image deconvolution algorithm with application to multi-frame and three-dimensional data. *J. Opt. Soc. Am. A. Opt. Image Sci. Vis.* **24**, 1580–1600.

Juskaitis, R. (2007) Characterizing high numerical aperture microscope objective lenses. In: *Optical Imaging and Microscopy: Techniques and Advanced Systems* (ed. by P. Torok & F.-J. Kao). Springer Verlag, Berlin.

Kam, Z., Hanser, B., Gustafsson, M.G., Agard, D.A. & Sedat, J.W. (2001) Computational adaptive optics for live three-dimensional biological imaging. *Proc. Natl. Acad. Sci. USA* **98**, 3790–3795.

Kam, Z., Kner, P., Agard, D. & Sedat, J.W. (2007) Modelling the application of adaptive optics to wide-field microscope live imaging. *J. Microsc.* **226**, 33–42.

Marsh, P.N., Burns, D. & Girkin, J.M. (2003) Practical implementation of adaptive optics in multiphoton microscopy. *Opt. Exp.* **11**, 1123–1130.

Murray, J.M., Appleton, P.L., Swedlow, J.R. & Waters, J.C. (2007) Evaluating performance in three-dimensional fluorescence microscopy. *J. Microsc.* **228**, 390–405.

Newman, A.A. (1968) *Glycerol*. C.R.C. Press, Cleveland, Ohio.

Poland, S.P., Wright, A.J. & Girkin, J.M. (2008) Active focus locking in an optically sectioning microscope utilizing a deformable membrane mirror. *Opt. Lett.* **33**, 419–421.

Potsaid, B., Bellouard, Y. & Wen, J.T. (2005) Adaptive scanning optical microscope (ASOM): a multidisciplinary optical microscope design for large field of view and high resolution imaging. *Opt. Exp.* **13**(18), 6504–6518.

Rueckel, M., Mack-Bucher, J.A. & Denk, W. (2006) Adaptive wavefront correction in two-photon microscopy using coherence-gated wavefront sensing. *Proc. Natl. Acad. Sci. USA* **103**, 17137–17142.

Schwertner, M., M.J.B., Neil, M.A.A. & Wilson, T. (2004) Measurement of specimen-induced aberrations of biological samples using phase stepping interferometry. *J. Microsc.* **213**, 11–19.

Shaevitz, J.W. & Fletcher, D.A. (2007) Enhanced three-dimensional deconvolution microscopy using a measured depth-varying point-spread function. *J. Opt. Soc. Am. A. Opt. Image Sci. Vis.* **24**, 2622–2627.

Shaner, N.C., Steinbach, P.A. & Tsien, R.Y. (2005) A guide to choosing fluorescent proteins. *Nat. Meth.* **2**, 905–909.

Sherman, L., Ye, J.Y., Albert, O. & Norris, T.B. (2002) Adaptive correction of depth-induced aberrations in multiphoton scanning microscopy using a deformable mirror. *J. Microsc.* **206**, 65–71.

Staudt, T., Lang, M.C., Medda, R., Engelhardt, J. & Hell, S.W. (2007) 2,2′-thiodiethanol: a new water soluble mounting medium for high resolution optical microscopy. *Microsc. Res. Tech.* **70**, 1–9.

Swedlow, J.R., Sedat, J.W. & Agard, D.A. (1997) Deconvolution in Optical Microscopy. In: *Deconvolution of Images and Spectra* (ed. by P.A. Jansson). 2nd edn. Academic Press, Inc., San Diego, California.

Tsai, P.S., Migliori, B., Campbell, K., Kim, T.N., Kam, Z., Groisman, A. & Kleinfeld, D. (2007) Spherical aberration correction in nonlinear microscopy and optical ablation using a transparent deformable membrane. *Appl. Phys. Lett.* **91**, 191102–191103.

Wolff, T. (2000) Histological techniques for the drosophila eye. Part I: larva and pupa. *Drosophila Protocols* (ed by W. Sullivan, M. Ashburner & R.S. Hawley). 1st edn. Cold Spring Harbor Laboratory Press, New York.

Wright, A.J., Patterson, B.A., Poland, S.P., Girkin, J.M., Gibson, G.M. & Padgett, M.J. (2006) Dynamic closed-loop system for focus tracking using a spatial light modulator and a deformable membrane mirror. *Opt. Exp.* **14**, 222–228.

Wright, A.J., Poland, S.P., Girkin, J.M., Freudiger, C.W., Evans, C.L. & Xie, X.S. (2007) Adaptive optics for enhanced signal in CARS microscopy. *Opt. Exp.* **15**, 18209–18219.

Wyckoff, J.B., Wang, Y., Lin, E.Y., *et al.* (2007) Direct visualization of macrophage-assisted tumor cell intravasation in mammary tumors. *Cancer Res.* **67**, 2649–2656.

